IEEE Access
Multidisciplinary | Rapid Review | Open Access Journal

Received 11 November 2023, accepted 5 December 2023, date of publication 12 December 2023,
date of current version 15 December 2023.

Digital Object Identifier 10.1109/ACCESS.2023.3341703

RESEARCH ARTICLE

Nonlinear Adaptive Disturbance Rejection Control Strategy Based on VSG for Photovoltaic-Storage Grid-Connected Inverter

FANNIE KONG[1], HAOCHEN ZHANG[1], WU ZHUOLIN[1], AND GUO ZHUANGZHI[2]
[1]School of Electrical Engineering, Guangxi University, Nanning, Guangxi 530005, China
[2]School of Electrical Information Engineering, Henan University of Engineering, Zhengzhou 450051, China

Corresponding author: Fannie Kong (kongfannie@163.com)

This work was supported in part by the National Natural Science Foundation of China under Grant 61861003, in part by the Guangxi Natural Science Foundation under Grant 2021GXNSFAA220136, and in part by the Young Scientists Fund of the National Natural Science Foundation of China under Grant 51707057.

ABSTRACT In this paper, a nonlinear adaptive disturbance rejection control (NADRC) strategy is designed to overcome the limitations of the traditional virtual synchronous generator (VSG) control method in photovoltaic (PV) grid-connected energy storage systems. This strategy utilizes exact feedback linearization and linear optimal control theory to establish a nonlinear adaptive disturbance rejection control law based on the virtual synchronous generator. It achieves zero static error control and noise adaptive stabilization of the AC link in a multiple-input multiple-output system. Compared with the simulation results of the grid-connected inverter voltage and current double closed-loop (VACDCL) strategy, the nonlinear adaptive disturbance rejection control effectively mitigates the fluctuations in load current caused by the photovoltaic energy storage module. It ensures power tracking under variable power conditions and outperforms traditional PI dual-loop control in terms of dynamic and static regulation performance as well as grid-connected current quality. Furthermore, this strategy's anti-disturbance adaptive link can quickly respond to system disturbances like frequency drift, voltage oscillations, and load current variations, thereby improving system performance.

INDEX TERMS Adaptive, exact feedback linearization, grid-connected inverter, multi-input multi-output, nonlinear adaptive disturbance rejection control, virtual synchronous generator, voltage and current dual closed-loop strategy.

I. INTRODUCTION

With the wide application of photovoltaic (PV) power plants, renewable energy is fully utilized while inevitably impacting the grid stability due to its volatility and uncertainty [1]. In addition, the voltage rise and fall system between the PV power unit and the grid will worsen the grid stability and robustness, so the power shall be converted through the grid-connected inverter again before feeding into the grid. However, conventional inverters lack inertia and damping, and can hardly achieve decentralized autonomous operation.

The associate editor coordinating the review of this manuscript and approving it for publication was Mohd Tariq.

The virtual synchronous generator (VSG), as a flexible grid-connected inverter, has been increasingly used in engineering practice because of its superior characteristics, such as voltage regulation, frequency regulation, and inertia damping of synchronous generators [2], [3], [4], [5], [6], [7]. However, the regulation accuracy of PI double loop in traditional VSG control is insufficient, and when the system operating point deviates from the initial equilibrium point by a large range, the PI parameters of the controller may not meet the current performance requirements and thus the system oscillates [8]. To ensure the stable operation of the grid, finding an efficient, stable, and safe means of VSG control has become an important research direction.

In the control of grid-connected inverter, droop control and voltage and current double closed-loop control are usually used. However, the adjustment ability of this strategy to the dynamic and static performance of the new energy grid-connected system is low, and the control accuracy is low. For this situation, an improved voltage and current double closed-loop (VACDCL) strategy based on sequence control and second-order generalized integrator was designed [9]. By separating the positive and negative sequence components of voltage, the unbalance of output voltage under unbalanced load condition is reduced. In addition, in the integrated compensation VSG control strategy, the frequency deviation caused by load disturbance is eliminated by the parallel integration compensator on the damping coefficient D [10], which improves the frequency modulation performance of the VSG system and inhibits the power oscillation of the VSG system. However, the experimental results of VSG voltage regulation capability and power quality are lacking. In addition, some scholars have designed an adaptive VSG control strategy by using the root locus method and time domain analysis method [11]. The strategy uses adaptive virtual inertia and adaptive sag gain to improve the additional oscillation caused by low power consumption in the battery energy storage system. At the same time, based on the fourth-order generator model, an adaptive terminal sliding mode control law has been proposed and can realize the static error-free control of VSG analog excitation link, effectively overcoming the influence of filter parameter uncertainty and improving system stability [12]. A nonlinear control strategy of inverter based on reactive voltage drop control is proposed to reduce the reactive power sharing error and improve the voltage stabilization performance of the system. Based on the analysis of single-phase grid-connected inverters, some scholars have used the state-space method, phase diagram, and bifurcated diagram to prove that the dynamic performance of the system is closely related to the parameters of the nonlinear predictive controller [14]. In terms of the nonlinearization of VSG power Angle characteristics and the setting of active power control parameters in grid-connected mode, [15] and [16] select the relative maximum power coefficient in the optional domain through the configuration of extreme value points to improve the stability of the system. Similarly, a team designed an adaptive controller based on the depth deterministic strategy gradient algorithm to adapt the internal parameters of the system, so that the system has stronger anti-interference performance and dynamic and static adjustment performance [17]. However, it does not consider the strong volatility of new energy under the premise of grid connection. Therefore, to solve the problem of low reliability of photovoltaic battery energy storage systems, a VSG control strategy based on voltage frequency control was proposed. The output power of VSG is adjusted by changing the position of the primary frequency modulation curve, and the voltage component is superimposed on the voltage loop to balance the DC power and AC power of the inverter. Aiming at the power oscillation and current imbalance in the VSG system, an output cascade control strategy based on improved VSG is proposed [18]. By adding a positive and negative sequence current regulator in the control link, the output current balance is realized and the power fluctuation is reduced effectively. However, the stability of the system under power disturbance or voltage disturbance is ignored. Some integrated control strategies [19], [20], [21] that combine traditional VSG control algorithms and classical algorithms are limited to highly linearized models, although the problem of power Constance under unbalanced voltage conditions is considered. When the system is disturbed by high-frequency signals, the control performance of the controller will be reduced, and the system will lose stability. To solve this problem, a nonlinear control law [23] has been designed by applying the precise linearization of state feedback to the nonlinear decoupling control of the converter [22] or using the sliding mode control [24]. These control strategies can realize the decoupling control of active power and reactive power according to the characteristics of strong nonlinear and high coupling degree of photovoltaic inverters, and improve the transient response speed and robustness of the system, but only consider the isolated island operation of the system, and lack the interference test simulation results of the system. The state quantities in the mathematical model of three-phase grid-connected VSG are all AC quantities, and there is a strong coupling between variables, so VACDCL is commonly used to decouple them [25], [26]. However, when VACDCL is used as the underlying control strategy, the controller actually indirectly modulates the feedback signal and cannot adjust the given AC voltage and current signal without static difference [28], [29]. Because the PI parameters in VACDCL are mostly selected by empirical method [30], the PI parameters optimized by intelligent algorithm also have the problem of complicated calculation [34]. In addition, the PI parameters obtained by theoretical calculation differ greatly from the actual engineering parameters, which cannot meet the current performance adjustment requirements of rapid response [30], [31].

In order to solve the problems of poor dynamic and static performance and poor robustness under disturbance conditions of the traditional VACDCL control, in this paper, a nonlinear adaptive disturbance rejection control (NADRC) strategy is designed to construct the input-output connection by nonlinear modeling of grid-connected VSG and is used to replace the traditional VACDCL. A Clark transform is applied to the new system model to design the inverter output voltage and its first-order derivatives as the output function and the switching signals as the input function to establish the connection between the input and output variables. The designed NADRC strategy is introduced into the control of the VSG to regulate the dynamic and static performance of the system. The anti-interference performance of the system is improved by introducing an adaptive function. Meanwhile, the output and feedback coefficient matrices of the system are optimized according to the zero-pole criterion to improve the overall performance of the system.

Finally, the superiority of the strategy is verified by simulation.

In this paper, the construction process of the PV energy storage model and the nonlinear modeling at the VSG grid-connected points are presented in Section II. Subsequently, Section III describes in detail the design idea of the NADRC strategy proposed in this paper. In Section IV this paper presents simulation simulations comparing the proposed control strategy with the conventional VACDCL under different disturbance conditions on the system. Finally, Section V gives the final conclusion of this work.

II. VSG-BASED SYSTEM NONLINEAR CONTROL MODEL

A. VSG PV ENERGY STORAGE PRE-STAGE MODEL

The PV energy storage grid-connected VSG control system generally consists of two-stage modules. The front-stage module contains a PV module and an energy storage module to keep the bus voltage constant (Fig. 1). The rear module is the VSG control module, which is used to invert and maintain system stability. The PV module output voltage control method is maximum power point tracking. Given the topological complexity of the power system and the diversity of photovoltaic storage access to the grid, a Maximum Power Point Tracking (MPPT) strategy under uniform irradiance conditions is used to facilitate system construction. The control means of this link is perturbation observation with variable steps, and its specific control block diagram is shown in Fig. 2, where $U(k)$, $I(k)$, and $P(k)$ are the voltage, current, and power at time k, respectively, U is the operating point voltage, U_m is the maximum power point voltage, ΔU_1 and ΔU_2 are the large and small voltage steps respectively, and l is the reference step. In the beginning, ΔU_1 is used to quickly approach U_m, while in the process, the absolute value of the difference between U and U_m is calculated. When the absolute value is larger than l, ΔU_1 is used. Otherwise, ΔU_2 is adopted. At this time, the working point will slightly fluctuate near and eventually stabilize at U_m. This method ensures the speed and accuracy of the maximum power point tracking and reduces the energy loss of the system.

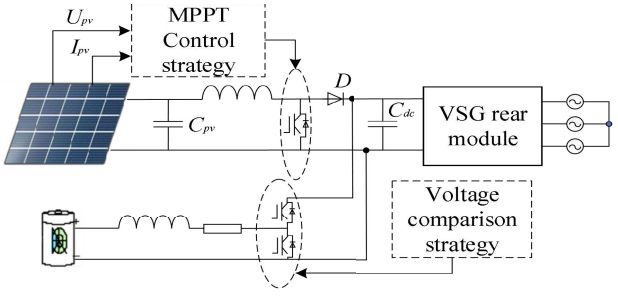

FIGURE 1. VSG structure diagram of PV energy storage grid connection.

Owing to its high volatility and low adjustability, the PV energy output does not have the characteristics of prime movers, so it must be equipped with an energy storage system on the DC side to achieve the PV -VSG technology. Hence, we designed an energy storage system composed of a battery and a boost converter to send the PV output voltage to the latter module after regulation. The battery as an energy storage device can reduce the impact of power disturbance and load disturbance of the micro source on the grid. The DC voltage output from the PV module is connected via a boost circuit to the bi-directional DC-DC converter of the battery storage link, thus stabilizing the voltage on the DC bus at a given voltage.

B. GRID-CONNECTED INVERTER MODULE

For convenience in the subsequent study, a single infinity system is taken as an example. As shown in Fig. 3, U_{dc} is the upper-level PV DC output voltage; C_{dc} is the dc-side filter capacitor; E_{abc} is the no-load electric potential of each phase of the inverter; L_f and C_f are the filter inductor and filter capacitor, respectively; R_g and L_g are the series simulated grid impedance, and the inverter is modulated by Space vector pulse width modulation (SVPWM) [32].

From Fig. 3, the nonlinear state space equations for the PCC point are established according to Kirchhoff's voltage law (KVL) and Kirchhoff's Current Law (KCL):

$$\begin{cases} L_{f_1}\dot{i}_{1a} = (s_a - \frac{1}{3}\sum\limits_{k=a,b,c} s_k)U_{dc} - u_{ca} - R_f(i_{1a} - i_{2a}) \\ L_{f_1}\dot{i}_{1b} = (s_b - \frac{1}{3}\sum\limits_{k=a,b,c} s_k)U_{dc} - u_{cb} - R_f(i_{1b} - i_{2b}) \\ L_{f_1}\dot{i}_{1c} = (s_c - \frac{1}{3}\sum\limits_{k=a,b,c} s_k)U_{dc} - u_{cc} - R_f(i_{1c} - i_{2c}) \\ C_f\dot{u}_{ca} = i_{1a} - i_{2a} \\ C_f\dot{u}_{cb} = i_{1b} - i_{2b} \\ C_f\dot{u}_{cc} = i_{1c} - i_{2c} \end{cases} \tag{1}$$

where L_{f_1} and C_f are the filter inductor and filter capacitor of VSG, respectively, $S_{k=abc}$ is the switching signal array, U_{dc} is the DC side capacitance-voltage, i_{1_a}, i_{1_b}, and i_{1c} are the three-phase current of the inverter output, i_{2_a}, i_{2_b} and i_{2_c} are the current at the grid connection end of VSG, and u_{ca}, u_{cb} and u_{cc} are the voltage drop at the grid connection point of VSG.

The conventional VACDCL control requires the state quantities in (1) to be Park-transformed to the rotating $dq0$ coordinate system. However, the cross-coupling term containing ω is introduced in the voltage and current components after the Park transformation, which complicates the subsequent study [27], so the Clark transformation with constant transformation coefficients is chosen [33]:

$$\begin{cases} C_f\dot{u}_{c\alpha} = i_{1\alpha} - i_{2\alpha} \\ C_f\dot{u}_{c\beta} = i_{1\beta} - i_{2\beta} \\ L_{f_1}\dot{i}_{1\alpha} = s_\alpha U_{dc} - u_{c\alpha} - R_f(i_{1\alpha} - i_{2\alpha}) \\ L_{f_1}\dot{i}_{1\beta} = s_\beta U_{dc} - u_{c\beta} - R_f(i_{1\beta} - i_{2\beta}) \end{cases} \tag{2}$$

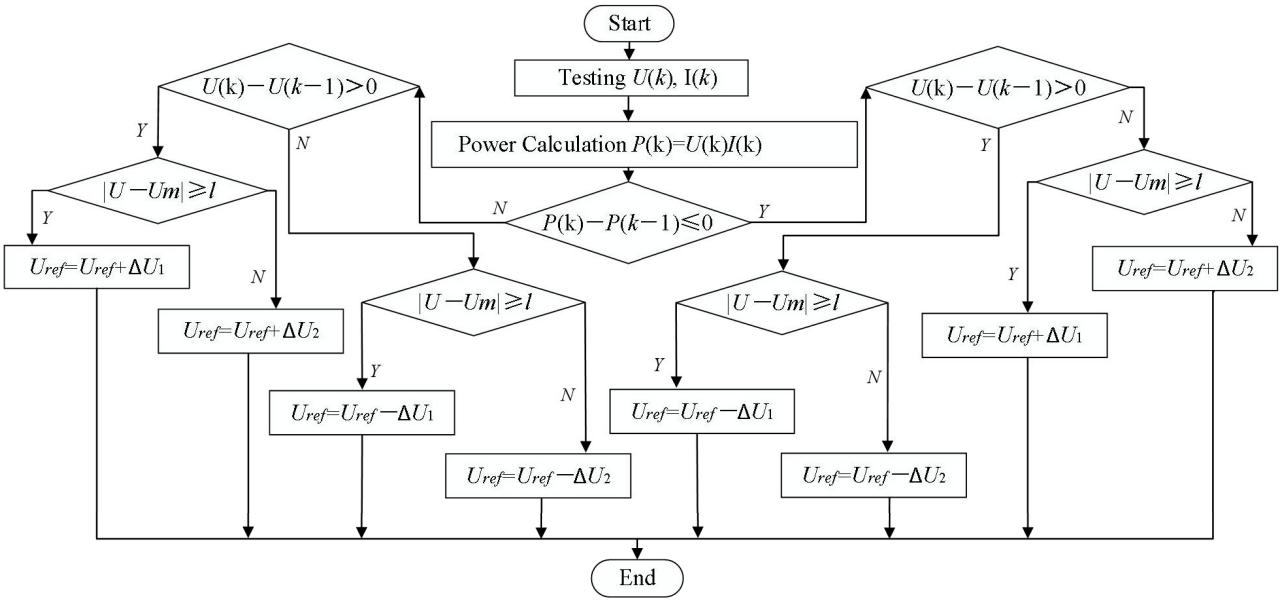

FIGURE 2. Disturbance observation method control block diagram.

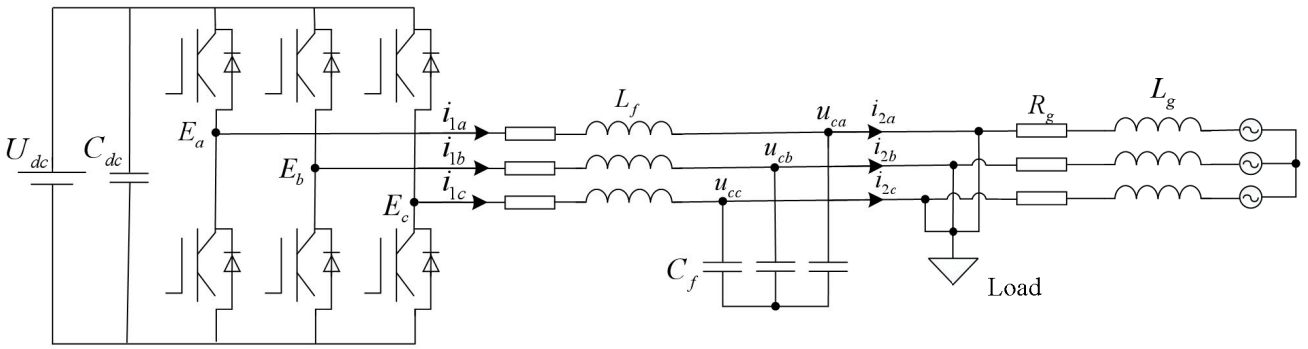

FIGURE 3. VSG post-module circuit diagram.

(2) can be translated into a VSG model in a nonlinear state space as follows:

$$Z_0\dot{x} = A_0x + B_{10}u + B_{20}w \tag{3}$$

where $x = [u_{c\alpha}, u_{c\beta}, i_{1\alpha}, i_{1\beta}]^T$ is the state vector, $u = [u_\alpha, u_\beta]^T$ is the control vector, $w = [d_\alpha, d_\beta]^T$ is the perturbation vector, $Z_0 = diag[C_f, C_f, L_{f_1}, L_{f_1}]^T$ is the impedance matrix, A_0 is the state matrix, B_{10} is the perturbation matrix, and B_{20} is the control matrix.

(2) and (3) are combined to organize the state space mathematical model of the system:

$$\begin{cases} \dot{x}_1 = \dfrac{1}{C_f}x_3 - \dfrac{1}{C_f}d_1 \\ \dot{x}_2 = \dfrac{1}{C_f}x_4 - \dfrac{1}{C_f}d_2 \\ \dot{x}_3 = -\dfrac{1}{Lf}x_1 - \dfrac{R_f}{L_f}x_3 + \dfrac{U_{dc}}{L_f}u_1 \\ \dot{x}_4 = -\dfrac{1}{Lf}x_2 - \dfrac{R_f}{L_f}x_4 + \dfrac{U_{dc}}{L_f}u_2 \end{cases} \tag{4}$$

C. VSG MODEL ANALYSIS

From the main circuit structure diagram of the system shown in Fig. 1, the fast electromagnetic transient process of the grid-connected inverter is used to simulate the electromechanical transient process of the synchronous generator according to the basic VSG theory, as shown in the block diagram in Fig. 4.

As shown in Fig. 4, P_m and P_e are the active power set value P_{ref} and the active power feedback P at the PCC respectively; D and J are the virtual damping and virtual rotational inertia respectively.

Referring to the excitation link of the synchronous generator, VSG reactive power-voltage droop control is designed:

$$\frac{k_{iq}}{s}\left[D_q(U - U_{ref}) + Q - Q_{ref}\right] = E_0 \tag{5}$$

where k_{iq} is the integral coefficient, D_q is the reactive power-droop coefficient; U is the voltage feedback value at the parallel network; U_{ref} is the voltage setting value at the machine end; Q is the reactive power feedback at the

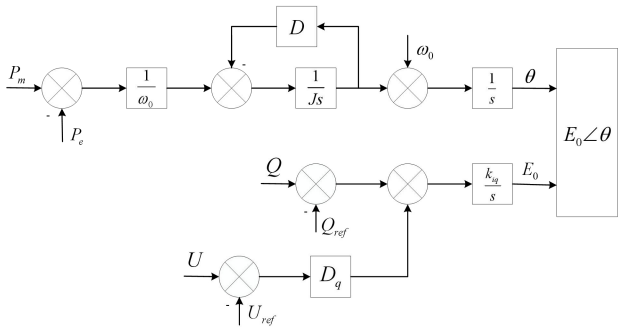

FIGURE 4. Terminal voltage synthesis block diagram of VSG.

parallel network; Q_{ref} is the reactive power setting value; E_0 is the no-load electric potential amplitude of VSG.

D. ANALYSIS OF VSG NADRC MODEL

The VSG NADRC model is shown in Fig. 5. The detected three-phase voltage and current at the parallel network, u_{cabc} and i_{cabc} are Clark-transformed to obtain the components $u_{c\alpha\beta}$ and $i_{c\alpha\beta}$ on the $\alpha\beta 0$ coordinate axis. The instantaneous value of the inverter output three-phase voltage, E_0, can be obtained from (9) and (10). The reference values obtained are compared with the actual detected values and fed to the nonlinear controller to obtain the inverter switching signals $u_{c\alpha}$ and $u_{c\beta}$, which are modulated by *SVPWM*.

III. DESIGN OF NADRC STRATEGY BASED ON VSG

A. DESIGN OF NADRC

The model output equation is constructed from (6):

$$\begin{cases} y_1 = c_1(x_1 - x_{10}) + c_2(\dot{x}_1 - \dot{x}_{10}) \\ y_2 = c_3(x_2 - x_{20}) + c_4(\dot{x}_2 - \dot{x}_{20}) \end{cases} \tag{6}$$

where x_{10} and x_{20} are the reference values of the VSG parallel network voltage in the $\alpha\beta 0$ coordinate system; $\dot{x}_{10}$ and $\dot{x}_{20}$ are the first-order derivative functions of the reference values. The interference term d_1 and d_2 are as zero, and (4) and (6) are combined to obtain the affine nonlinear model of the system:

$$\begin{cases} \dot{x} = f(x) + M_1(x)u_1 + M_2(x)u_2 \\ y_1 = I_1(x) \\ y_2 = I_2(x) \end{cases} \tag{7}$$

where $f(x) = Z_0^{-1}A_0$ is a 4×1 dimensional input matrix; $M_1(x)$ and $M_2(x)$ are both 4×1 dimensional control matrices; u_1 and u_2 are scalar control functions; $I_1(x)$ and $I_2(x)$ are scalar output functions, where:

$$\begin{aligned} M_1(x) &= \begin{bmatrix} 0 & 0 & \dfrac{U_{dc}}{L_{f_1}} & 0 \end{bmatrix}^T \\ M_2(x) &= \begin{bmatrix} 0 & 0 & 0 & \dfrac{U_{dc}}{L_{f_1}} \end{bmatrix}^T \end{aligned} \tag{8}$$

The Lie brackets of $M_1(x)$ and $M_2(x)$ vector fields for $f(x)$ defined by (8) are:

$$\begin{cases} [f, M_1] = \dfrac{\partial M_1(x)}{\partial x} f(x) - \dfrac{\partial f(x)}{\partial x} M_1(x) \\ [f, M_2] = \dfrac{\partial M_2(x)}{\partial x} f(x) - \dfrac{\partial f(x)}{\partial x} M_2(x) \end{cases} \tag{9}$$

According to Frobenius' theorem, there is a smooth vector field such as:

$$\begin{aligned} M_\Delta(x) &= [M_1(x), M_1(x), [f, M_1], [f, M_2]] \\ &= \begin{bmatrix} 0 & 0 & -\dfrac{U_{dc}}{L_{f_1} C_f} & 0 \\ 0 & 0 & 0 & -\dfrac{U_{dc}}{L_{f_1} C_f} \\ \dfrac{U_{dc}}{L_{f_1}} & 0 & \dfrac{R_f}{L_{f_1} C_f} & 0 \\ 0 & \dfrac{U_{dc}}{L_{f_1}} & 0 & \dfrac{R_f}{L_{f_1} C_f} \end{bmatrix} \end{aligned} \tag{10}$$

Since the rank of $M_\Delta(x)$ is 4=n, the distribution space Δx is involutory in the neighborhood U of x; that is, the system can achieve state feedback linearization.

Next, the relative order of the system is determined. From Kirchhoff's law, the VSG and the relationship at the network are obtained:

$$\begin{cases} \ddot{x}_i = a\dot{x}_i + bu_i + gx_i + W \\ \ddot{x}_{i0} = a\dot{x}_{i0} + bu_i + gx_{i0} + W \end{cases} \quad (i = 1, 2) \tag{11}$$

where a, b and g are constant coefficients.

We have $W = \Delta a\dot{x} + \Delta bu + \Delta gx + \eta$, Δ is the system error caused by parameter perturbation, η is the load current disturbance, and W is the sum of the two uncertain disturbances; $|W| < \mu$, where μ is a positive real number.

From (11), it is obtained that:

$$\Delta\dot{x}_i = \dot{x}_i - \dot{x}_{i0} = \frac{\ddot{x}_i - \ddot{x}_{i0} - g(x_i - x_{i0})}{a} \tag{12}$$

where i = 1,2.

From (12), the difference of the first-order derivative in the output function is bounded and $|\Delta\dot{x}_i| < \rho$, where ρ is a very small real number.

From (10), the 2×2 matrix is obtained as follows:

$$\tilde{M}(x) = \begin{bmatrix} L_{M_1} L_f^1 I_1(x) & L_{M_2} L_f^1 I_1(x) \\ L_{M_1} L_f^1 I_2(x) & L_{M_2} L_f^1 I_2(x) \end{bmatrix} \tag{13}$$

The $\tilde{M}(x)$ in (13) is nonsingular, and its relative order is r=4=n. Therefore, the nonlinear model can achieve the following local diffeomorphism transformation. According to (13), the transformed Jacobian matrix is full rank, so the nonlinear system can achieve complete exact linearization.

$$\begin{aligned} z &= \begin{bmatrix} z_1 & z_2 & z_3 & z_4 \end{bmatrix}^T = \begin{bmatrix} y_1 & \dot{y}_1 & y_2 & \dot{y}_2 \end{bmatrix}^T \\ &= \begin{bmatrix} c_1(x_1 - x_{10}) + c_2(\dot{x}_1 - \dot{x}_{10}) \\ c_1(\dot{x}_1 - \dot{x}_{10}) \\ c_3(x_2 - x_{20}) + c_4(\dot{x}_2 - \dot{x}_{20}) \\ c_3(\dot{x}_2 - \dot{x}_{20}) \end{bmatrix} \end{aligned} \tag{14}$$

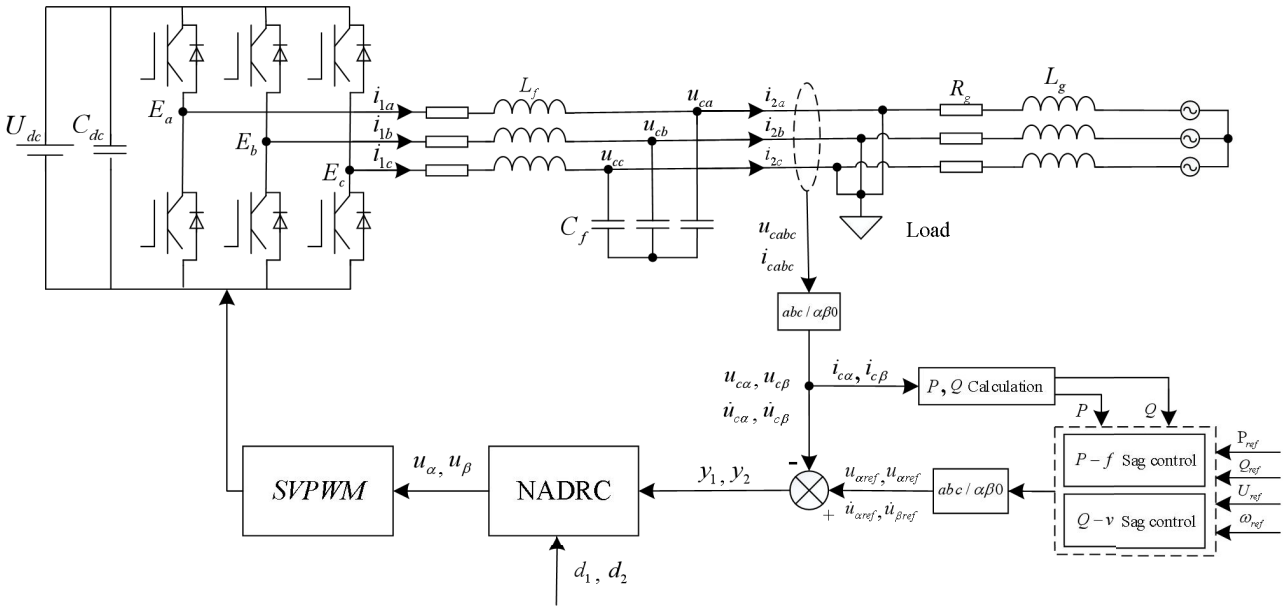

FIGURE 5. Block diagram of NADRC.

Combining (7) and (14) yields:

$$\begin{cases} \dot{z}_1 = c_1(\dot{x}_1 - \dot{x}_{10}) \\ \dot{z}_2 = \dfrac{c_1 U_{dc}}{L_{f_1} C_f} u_1 - \dfrac{c_1}{L_{f_1} C_f} x_1 - \dfrac{c_1 R_f}{L_{f_1} C_f} x_3 - c_1 \ddot{x}_{10} = v_1 \\ \dot{z}_3 = c_3(\dot{x}_2 - \dot{x}_{20}) \\ \dot{z}_4 = \dfrac{c_3 U_{dc}}{L_{f_1} C_f} u_2 - \dfrac{c_3}{L_{f_1} C_f} x_2 - \dfrac{c_3 R_f}{L_{f_1} C_f} x_4 - c_3 \ddot{x}_{20} = v_2 \end{cases} \tag{15}$$

where v_1, v_2 is the linear spatial feedback control law. Here the optimal control theory design can be used, and for the regulator, the quadratic performance index is selected as follows:

$$J = \frac{1}{2} \int_0^\infty (z^T Q z + v^T R v) dt \tag{16}$$

Solving the algebraic equations of the Rickati matrix yields the positive definite matrix P:

$$A^T P + PA - PBR^{-1} B^T P + Q = 0 \tag{17}$$

The control law of the z spatial linear system can be obtained according to (17):

$$v = -R^{-1} B^T P z = -Lz \tag{18}$$

where $\underset{2\times2}{L} = diag[l_1, l_2]$ is a positive real number matrix. Substituting (18) into (15) yields the control law on the nonlinear space of the system as follows:

$$\begin{cases} u_1 = \dfrac{L_{f_1} C_f}{c_1 U_{dc}} \left(\dfrac{c_1}{L_{f_1} C_f} x_1 + \dfrac{c_1 R_f}{L_{f_1} C_f} x_3 + c_1 \ddot{x}_{10} \right. \\ \qquad \left. - l_1 c_1 \Delta x_1 - l_1 c_2 \Delta \dot{x}_1 \right) \\ u_2 = \dfrac{L_{f_1} C_f}{c_3 U_{dc}} \left(\dfrac{c_3}{L_{f_1} C_f} x_2 + \dfrac{c_1 R_f}{L_{f_1} C_f} x_4 + c_3 \ddot{x}_{20} \right. \\ \qquad \left. - l_2 c_3 \Delta x_2 - l_2 c_4 \Delta \dot{x}_2 \right) \\ \Delta x_1 = x_1 - x_{10} \\ \Delta x_2 = x_2 - x_{20} \\ \Delta \dot{x}_1 = \dot{x}_1 - \dot{x}_{10} \\ \Delta \dot{x}_2 = \dot{x}_2 - \dot{x}_{20} \end{cases} \tag{19}$$

For the presence of external disturbance d, an adaptive disturbance rejection control law is set to overcome the uncertainty and the applied disturbance:

$$\begin{cases} u_{vw1} = -t_1 sat(v_1) - t_2 \hat{d}_1 sat(v_1) \\ u_{vw2} = -t_3 sat(v_2) - t_4 \hat{d}_2 sat(v_2) \end{cases} \tag{20}$$

where t_1, t_2, t_3 and t_4 are the switching gain constants, and $sat(v)$ is the saturation function of v. Combining (19) and (20) yields an NADRC law as follows:

$$\begin{cases} u_\alpha = u_1 + u_{vw1} \\ u_\beta = u_2 + u_{vw2} \end{cases} \tag{21}$$

B. PARAMETER SETTING OF NADRC

By expanding the Taylor series at the equilibrium point x_0 and taking a linear transformation, the nonlinear

system (4) can be transformed into a controllable standard form:

$$\begin{cases} \dot{x}_L = A_L x + B_L u \\ y = C_L x \end{cases} \tag{22}$$

where,

$$A_L = \begin{bmatrix} 0 & 0 & 0 & 1 \\ -b_1^{11} & -b_1^{11} & -b_1^{12} & -b_2^{12} \\ 0 & 0 & 0 & 1 \\ -b_1^{21} & -b_2^{21} & -b_2^{22} & -b_1^{22} \end{bmatrix},$$

$$B_L = \begin{bmatrix} 0 & 0 \\ 1 & 0 \\ 0 & 0 \\ 0 & 1 \end{bmatrix},$$

$$C_L = \begin{bmatrix} c_1 & 0 & c_2 & 0 \\ 0 & c_3 & 0 & c_4 \end{bmatrix}$$

According to the design idea of nonlinear control law and mathematical induction, the system feedback control law can be obtained as follows:

$$\begin{aligned} u &= (C_L A_L B_L)^{-1} (-C_L A_L x + v) \\ &= -\frac{C_L A_L^2 x + lkx}{C_L A_L B_L} \end{aligned} \tag{23}$$

where, $l = \begin{bmatrix} l_1 & 0 \\ 0 & l_2 \end{bmatrix}$, $k = \begin{bmatrix} C_{L1}^T & C_{L2}^T \end{bmatrix}^T$

The closed-loop control system can be obtained by combining (22) with (23):

$$\dot{x}_L = \frac{A_L - B_L lk}{C_L A_L B_L} x_L = V_L x_L \tag{24}$$

According to (24), it can be deduced:

$$V_L = \begin{bmatrix} 0 & 0 & 0 & 1 \\ 0 & 0 & -\frac{l_1 c_1}{c_2} & -l_1 - \frac{c_1}{c_2} \\ 0 & 0 & 0 & 1 \\ 0 & 0 & -\frac{l_2 c_3}{c_4} & -l_2 - \frac{c_3}{c_4} \end{bmatrix} \tag{25}$$

Then the characteristic equation of the system can be obtained from (25) as follows:

$$\left(s + \frac{c_1}{c_2}\right)\left(s + \frac{c_3}{c_4}\right)(s + l_1)(s + l_2) = 0 \tag{26}$$

According to (26) and the closed-loop characteristic root-zero pole assignment method, appropriate control parameters c and l can be selected to optimize the control effect of the system.

IV. SIMULATION VERIFICATON

In this section, we compared the conventional VACDCL with NADRC to verify the feasibility of the NADRC scheme. The simulations were performed in Matlab and Simulink. The solver is set to ode23t, the step is set to variable-step, and the switching frequency is set to 2500. The two control strategies are simulated in the same condition. All state variables of VSG are obtained from (4), input and output functions of NADRC are obtained from (6) and (7), and the system control law is given from (21). VACDCL refers to the traditional double-closed loop VSG model [27]. The control parameters of NADRC are given by (26) combined with the pole assignment method. The parameters of the simulation are shown in TABLE 1.

TABLE 1. System parameters.

U_{dc}(V)	800	F_0(Hz)	50	c_2	120000
L_f(mH)	0.8	U_n(V)	380	c_3	100
C_f(μF)	100	D_p	20	c_4	120000
R_f(Ω)	0.3	D_q	500	t_1	8×10^{-8}
R_g(Ω)	1.2	K_q	0.5	t_2	4×10^{-7}
L_g(mH)	1.2	l_1	8000	t_3	8×10^{-8}
D	500	l_2	8000	t_4	4×10^{-7}
J	0.5	c_1	10	γ	500
U_{dc}(V)	800	f_0(Hz)	50		

A. COMPARISON OF CURRENT MODULATION PERFORMANCE

Dynamic simulation of the VACDCL and the NADRC was carried out according to the simulation parameters. The simulation waveforms of grid-connected current in the same time segment were intercepted, and the modulation abilities of the two control strategies on the output current of the inverter were compared. TABLE 2 shows the frequencies and rates of the harmonic distortion of the grid-connected current of VACDCL and NADRC under different disturbance conditions. Clearly, the THDs of the two control strategies meet the requirements of harmonic content of grid-connected current, but the THDi% under the NADRC control decreases significantly (TABLE 2), indicating the power quality and dynamic performance of the system are both improved.

B. COMPARISON OF POWER TRACKING PERFORMANCE

Condition 1: Change of active power at the power grid end. The simulation results are shown in Fig. 6. Fig. 6(a) and Fig. 6(b) show the system active power and frequency change wave form under VACDCL and NADRC respectively when the given active power at the grid end increases by 20 KW at 1 s and decreases by 40 KW at 2 s. Within about 40 ms of the initial operation, the active power of the system

TABLE 2. Comparison of harmonic distortion rate of grid-connected current.

Strategies	THDi% for each perturbation			
	Active conversion	Frequency perturbation	Voltage disturbance	Single-phase short-circuit grounding
VACDCL	5.59	1.84	4.22	3.23
NADRC	4.97	1.68	4.06	2.89

under the VACDCL control oscillates violently, and the peaking value of the oscillation is 30.1 KW (Fig. 6(a)). This is because the load current generated by the PV energy storage module fluctuates greatly, while VACDCL does not consider the dynamic characteristics of the sub-module energy storage components. Active power and reactive power are still partially coupled under VACDCL, but NADRC can effectively solve this problem and form a smooth active power tracking curve. At $t = 1$ s, the set active power is increased by 20 KW, the peak time of the active power step response waveform under VACDCL control is 0.109 s, the overshot is 7.4%, and the setting time is 0.61 s. Under the NADRC control, the peak time of the active power step response waveform is 0.112 s, the overshot is 5.9%, and the setting time is 0.45 s. At $t = 2$ s, the set active power drops by 40 KW, the peak time of the active power step response waveform under the VACDCL control is 0.106 s, the overshot is 22.8%, and the setting time is 0.63 s. Under the NADRC control, the peak time of the active power step response waveform is 0.105 s, the overshoot is 19.1%, and the setting time is 0.46 s. Clearly, the transient of active power step response overjump and regulation time under the NADRC control are better than those of the VACDCL control. It is indicated the NADRC strategy not only achieves the complete decoupling of active power and reactive power but also endows the system with better dynamic and static performances. Due to the P-f droop control of VSG, when power disturbance occurs, the grid frequency changes accordingly, and the fast response of the set controller makes the grid frequency stabilize at the fundamental frequency in a very short time (Fig. 6(b)). At $t = 1$ s, the system frequency oscillates due to power rise. The peak value of the frequency waveform oscillation under the VACDCL control is 0.31 Hz, and the setting time is 0.76 s. The frequency waveform under the NADRC control is 0.25 Hz, and the setting time is 0.52 s. At $t = 2$ s, the system frequency oscillates due to a power drop. The peak value of frequency waveform oscillation under the VACDCL control is 0.60 Hz, and the setting time is 0.75 s. The peaking value of the frequency waveform under the NADRC control is 0.52 Hz, and the setting time is 0.51 s. The simulation results show that the NADRC control can achieve better frequency immunity performance than the VACDCL control when power disturbance occurs.

C. COMPARISION OF DISTURBANCE RESISTANCE

Condition 2: Power grid frequency drift. The simulation results are shown in Fig. 7. Fig. 7(a) and Fig. 7(b) show the

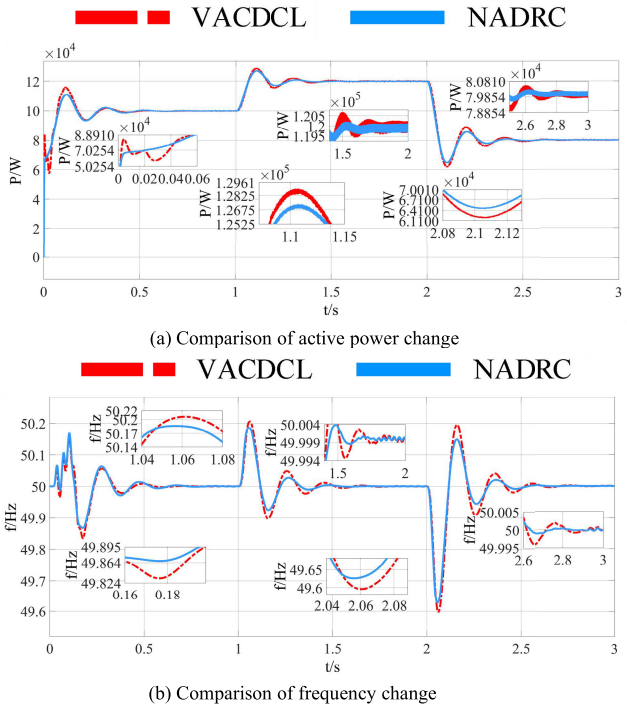

(a) Comparison of active power change

(b) Comparison of frequency change

FIGURE 6. Change the simulation result of the given active power.

system active power and frequency change waveform under the control of VACDCL and NADRC respectively when the frequency at the grid end drops by 0.25 Hz at 1 s and returns to the fundamental frequency at 2 s. At $t = 1$ s, the frequency continuously dropped by 0.25 Hz (Fig. 7(a)). Due to the P-f droop control of VSG, the system's active power was raised beyond the given active power and was finally maintained around 11 KW. At t=1 s, the peak time of the active power step response waveform under the VACDCL control is 0.071 s, the overshot is 9.4%, and the setting time is 0.75 s. Under the NADRC control, the peak time of the step response waveform is 0.068 s, the overshoot is 7.6%, and the setting time is 0.47 s. At $t = 2$ s, the frequency returns to 50 Hz, the peak time of the active power step response waveform 0.066 s, the overshot is 10.2%, and the setting time is 1.6 s. Under the NADRC control, the peak time of the active power step response waveform is 0.052 s, the overshot is 9.85%, and the setting time is 0.36 s. Thus, NADRC has better transient control performance in terms of recovery rate and fluctuation amplitude of active power under frequency disturbance. At t=1 s, the peak value of frequency waveform

oscillation under the VACDCL control is 0.168 Hz, and the setting time is 0.80 s (Fig. 7(b)). The peaking value of the frequency waveform under the NADRC control is 0.120 Hz, and the setting time is 0.59 s. Because the control parameters of VACDCL are not easy to set and the *PQ* is not completely decoupled, the performance indexes such as overshoot are difficult to optimize. Simulation results show the NADRC control strategy endows VSG with better frequency immunity performance.

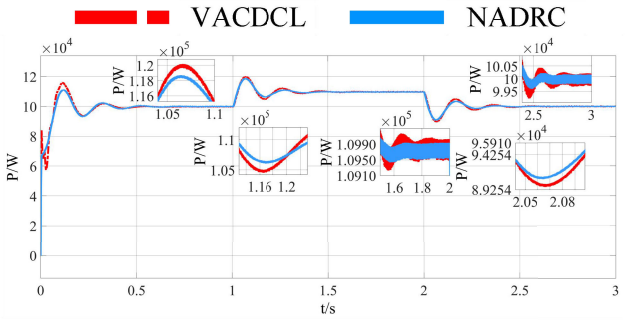

(a) Comparison of active power change

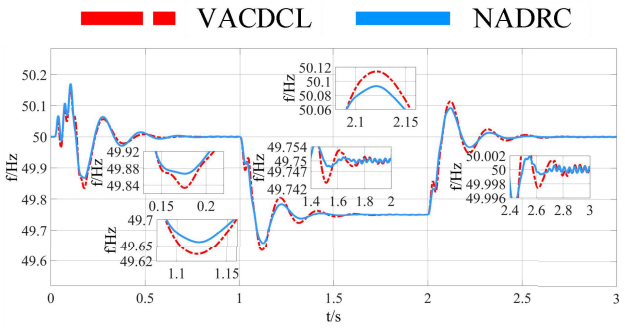

(b)Comparison of frequency change

FIGURE 7. Simulation results of power grid frequency decline.

Condition 3: Voltage disturbance. The simulation results are shown in Fig. 8. Fig. 8(a) and Fig. 8(b) show the system reactive power and DC bus voltage change waveform under the control of VACDCL and NADRC respectively when the grid terminal voltage drops at 1 s and rises at 2 s. Within 0.05 s of the initial operation under the VACDCL, the reactive power of the system oscillates greatly, and the amplitude of the oscillation is up to 5.7 kVar (Fig. 8(a)), which is caused by the incomplete decoupling of the active power and reactive power. In comparison, the amplitude of the reactive power oscillation under the NADRC control is small. Therefore, a relatively smooth reactive power tracing curve is obtained. At $t = 1$ s, the voltage at the grid end drops by 0.5 V. Moreover, because all the output power of the inverter is delivered to the grid, the voltage at the PCC is raised to exceed the rated voltage. In addition, due to the Q-v sag control and reactive power compensation, the reactive power output of VSG will be lower than the given value. At $t = 1$ s, the peak value of reactive power fluctuation is 5.72 kVar under VACDCL and 3.86 kVar under NADRC. At $t = 2$ s,

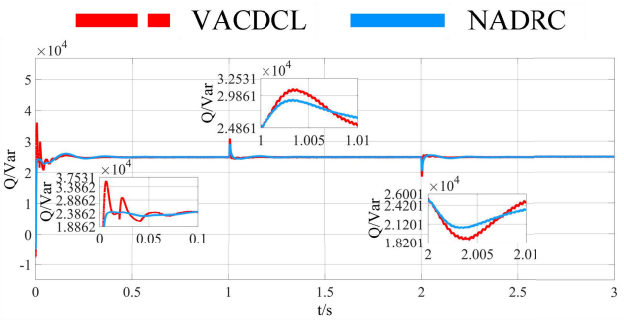

(a) Comparison of reactive power variation

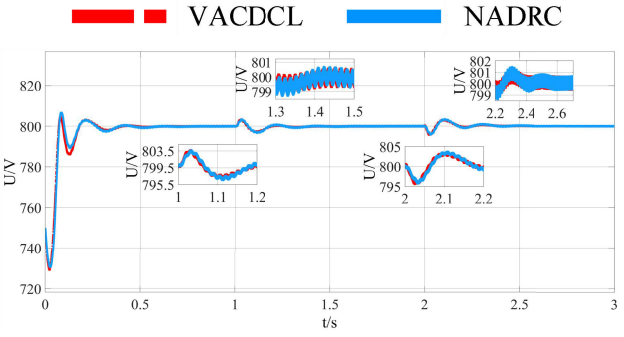

(b) Comparison of busbar voltage variation

FIGURE 8. Simulation results of grid voltage drop.

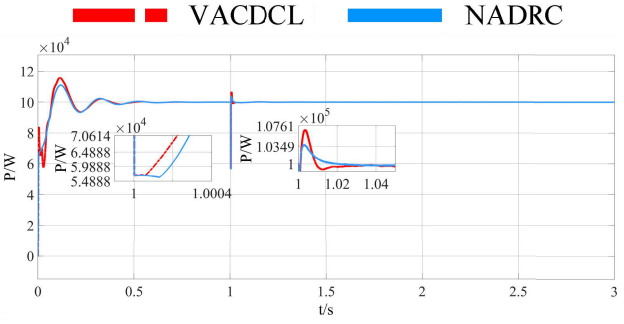

(a) Comparison of active power change

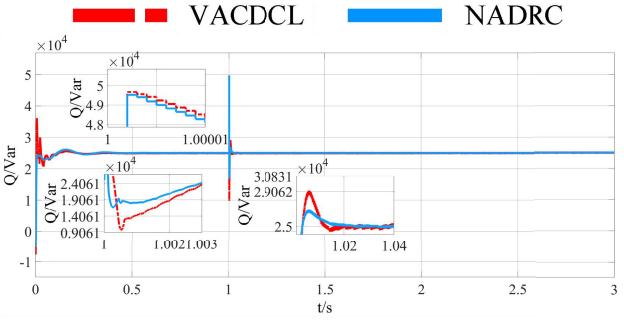

(b) Comparison of reactive power variation

FIGURE 9. Simulation results of single-phase short-circuit grounding.

the peak value of reactive power fluctuation is 6.14 kVar under VACDCL and 4.39 kVar under NADRC. The reason for the greater fluctuation amplitude under VACDCL is that the voltage drop of the power grid will cause a drop in the

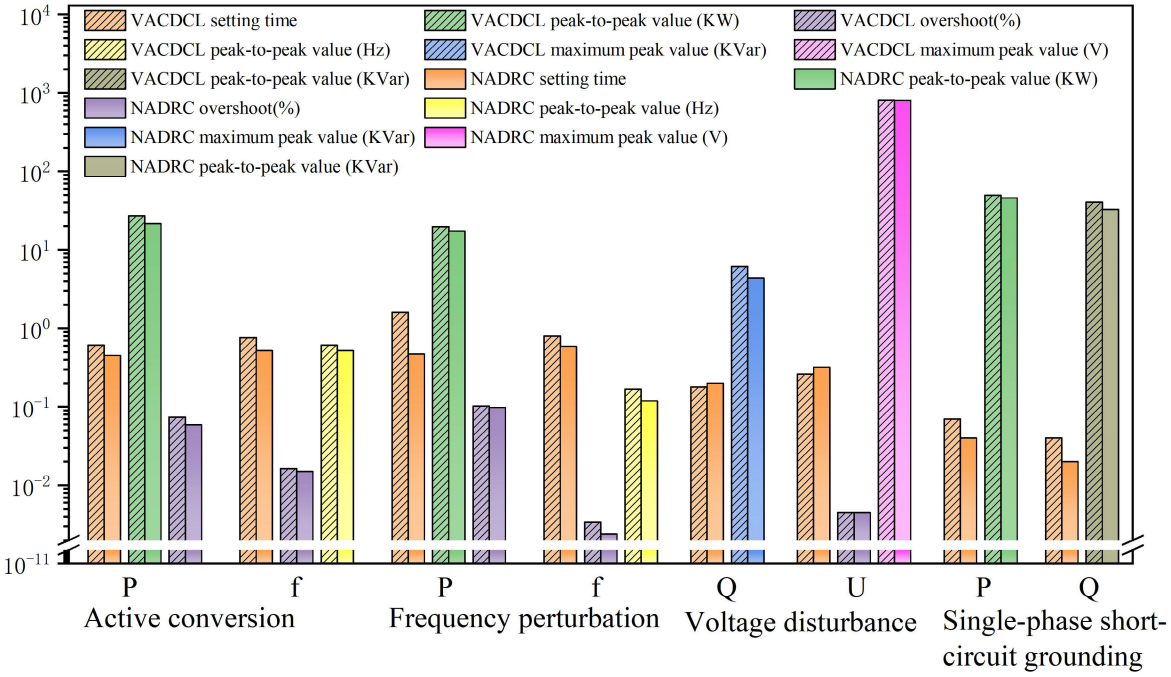

FIGURE 10. Comparison of VACDCL and NADRC performance indexes.

DC component of the energy storage component voltage and a fluctuation of other components. NADRC considers the decoupling of reactive power to voltage interference and thus has better transient control performance under voltage disturbance. As shown in Fig. 8(b), there is little difference between the voltage fluctuation changes of the two control strategies at 1 or 2 s, because the voltage regulation is completed by the pre-stage module and is little related to the control performance of the post-stage module. The simulation results show that the NADRC strategy endows the system with better voltage immunity performance.

Condition 4: Single-phase short-circuit grounding at the load end. The simulation results are shown in Fig. 9. Under the premise of constant power, the single-phase short-circuit grounding fault causes the system to generate a large pulse current at 1 s. Because the voltage fluctuation at the load side is not large, the active power and reactive power fluctuate greatly in a short time but will be re-adjusted to the steady state under the regulation of VSG. Single-phase short-circuit grounding occurs in the system at $t = 1$ s, and the peak fluctuation values of the active power and reactive power under VACDCL in a very short time are 51 kW and 39.8 kVar respectively (Fig. 9(a) and Fig. 9(b)). However, the peak values of active power and reactive power fluctuation of the system under NADRC in a very short time are 46 kW and 32.9 kVar respectively. This is because the NADRC strategy takes the load current as the disturbance term and adaptively adjusts this term. Therefore, when a system short-circuit fault occurs, the response speed of NADRC is faster than that of VACDCL. The system recovery overshoot is smaller, and the system converges to the steady state faster, thus reducing the impact of faults on the grid.

The comparison of specific performance indicators under four working conditions is shown in Fig. 10.

V. CONCLUSION

In order to solve the problem of poor tracking performance and anti-interference performance of traditional VSG control method under grid-connected photovoltaic energy storage, an effective NADRC law is designed to replace the traditional VACDCL strategy. The significance and novelty of this paper are as follows: First, this paper designs a pre-stage module of photovoltaic energy storage to replace the DC source part of the traditional VSG model, so that the operating environment of the system is more in line with the practical requirements of engineering. Secondly, the mathematical model of VSG at the PCC point is constructed, and a nonlinear adaptive disturbance rejection control strategy is designed to replace the traditional double closed-loop control strategy through multi-objective feedback theory and optimal control theory, combined with adaptive anti-interference variable function. Finally, the control matrix of the system is optimized by the pole assignment method to enhance the overall control performance of the system. The simulation results show that the NADRC strategy has good control performance. The NADRC strategy is compared with the VACDCL strategy under different interference conditions, and the effectiveness and superiority of the NADRC strategy in interference tracking and interference suppression are verified. NADRC also overcomes the problem that PI parameters cannot adapt to

the new system condition after perturbation and makes the convergence speed of the system adapt and improves the robustness. Finally, because of the consistency of the voltage and current regulation of the nonlinear link, the control quantity can be continuously output, the oscillation of the system is reduced, and the quality of the grid-connected current is improved.

The NADRC proposed in this paper can provide a new research idea for replacing the traditional VSG double closed-loop control strategy in the future. Although this strategy significantly improves the dynamic and static performance and disturbance immunity of VSG, due to the high degree of nonlinearization of NADRC, the parameter accuracy of its control matrix is required to be higher. In different system application scenarios, control parameters need to be adjusted according to different system models, so the complexity of real-time control is higher than that of VACDCL. Therefore, introducing intelligent algorithms, such as deep learning algorithms, into the tuning process of the NADRC control parameter matrix will be a new research idea for our future research. At the same time, since NADRC is a control strategy based on the nonlinear modeling of the system itself, the overall stability and robustness of the system can be guaranteed under the premise of appropriate control parameters and complete model data. Therefore, the model construction and parameter selection of complex power systems in multi-inverter and multi-machine scenarios will be deeply explored in future work.

REFERENCES

[1] Y. Zhang, T. Ma, and H. Yang, "Grid-connected photovoltaic battery systems: A comprehensive review and perspectives," *Appl. Energy*, vol. 328, Dec. 2022, Art. no. 120182.
[2] H. Wu, X. B. Ruan, D. S. Yang, X. R. Chen, Q. C. Zhong, and Z. P. Lv, "Modeling and parameter design of virtual synchronous generator power loop," *Chin. J. Elect. Eng.*, vol. 35, no. 24, pp. 6508–6518, 2015.
[3] P. Yang, Z. Chen, and T. Luo, "Control method of photovoltaic power generation and hybrid energy storage based on VSG," *Grid Clean Energy*, vol. 39, no. 2, pp. 83–91 and 113, 2023.
[4] J. Cheng and Z. M. Zhao, "Research on flexible control strategy of solid state transformer AC port based on virtual synchronous generator," *Power Syst. Protection Control*, vol. 51, no. 4, pp. 138–147, 2023.
[5] X. Zhang, L. Gong, X. Zhao, R. Li, L. Yang, and B. Wang, "Voltage and frequency stabilization control strategy of virtual synchronous generator based on small signal model," *Energy Rep.*, vol. 9, pp. 583–590, Apr. 2023.
[6] W. Sang, W. Guo, S. Dai, C. Tian, S. Yu, and Y. Teng, "Virtual synchronous generator, a comprehensive overview," *Energies*, vol. 15, no. 17, p. 6148, Aug. 2022.
[7] J. Chen, X. Zhang, Y. Yang, J. Chen, and X. Chen, "Impedance modelling and grid integration stability evaluation of three-phase virtual synchronous generator," *IET Power Electron.*, vol. 15, no. 1, pp. 80–91, Jan. 2022.
[8] P. Li, B. Wang, and S. C. Zhao, "Adaptive sliding mode control strategy under virtual synchronous generator in microgrid," *Elect. Automat.*, vol. 39, no. 3, pp. 86–89, 2017.
[9] Y. Zhu, H. Wang, and Z. Zhu, "Improved VSG control strategy based on the combined power generation system with hydrogen fuel cells and super capacitors," *Energy Rep.*, vol. 7, pp. 6820–6832, Nov. 2021.
[10] Z. B. Zhu, C. Y. Zhang, and X. B. Zeng, "Research on VSG control strategy of microgrid inverter based on integral compensation," *Control Eng.*, vol. 28, no. 5, pp. 979–983, 2021.
[11] P. He, Z. Li, H. Jin, C. Zhao, J. Fan, and X. Wu, "An adaptive VSG control strategy of battery energy storage system for power system frequency stability enhancement," *Int. J. Electr. Power Energy Syst.*, vol. 149, Jul. 2023, Art. no. 109039.
[12] B. B. Yan and B. H. Wang, "VSG control based on adaptive terminal sliding mode control method," *Electr. Power Automat. Equip.*, vol. 38, no. 10, pp. 140–146, 2018.
[13] F. Zandi, B. Fani, and A. Golsorkhi, "A visually driven nonlinear droop control for inverter-dominated islanded microgrids," *Electr. Eng.*, vol. 102, no. 3, pp. 1207–1222, Sep. 2020.
[14] Z.-X. Liao, D. Luo, X.-S. Luo, H.-S. Li, Q.-Q. Xiang, G.-X. Huang, T.-H. Li, and P.-Q. Jiang, "Nonlinear model and dynamic behavior of photovoltaic grid-connected inverter," *Appl. Sci.*, vol. 10, no. 6, p. 2120, Mar. 2020.
[15] H. Li, K. Wang, Z. Chen, H. Peng, and M. Tan, "Parameters design in active power control of virtual synchronous generator considering power-angle characteristic nonlinearity," *Int. J. Electr. Power Energy Syst.*, vol. 130, Sep. 2021, Art. no. 106952.
[16] K. Xiong, W. Hu, G. Zhang, Z. Zhang, and Z. Chen, "Deep reinforcement learning based parameter self-tuning control strategy for VSG," *Energy Rep.*, vol. 8, pp. 219–226, Aug. 2022.
[17] X. Yan, C. Wang, Z. Wang, H. Ma, B. Liang, and X. Wei, "A united control strategy of photovoltaic-battery energy storage system based on voltage-frequency controlled VSG," *Electronics*, vol. 10, no. 17, p. 2047, Aug. 2021.
[18] J. Cheng, Z. M. Zhao, L. Zhang, and S. Liang, "VSG-SST control strategy under unbalanced voltage conditions," *J. Sol. Energy*, vol. 44, no. 3, pp. 393–400, 2023.
[19] T. Zheng, L. Chen, Y. Guo, and S. Mei, "Comprehensive control strategy of virtual synchronous generator under unbalanced voltage conditions," *IET Gener., Transmiss. Distrib.*, vol. 12, no. 7, pp. 1621–1630, Apr. 2018.
[20] C. L. Dang, Q. Tong, W. Z. Song, and D. Liu, "Current sliding mode control strategy of LCL filter three-phase grid-connected inverter," *Power Electron. Technol.*, vol. 55, no. 6, pp. 1–4, 2021.
[21] S. Li, Y. Li, X. Chen, W. Jiang, X. Li, and T. Li, "Control strategies of grid-connection and operation based on active disturbance rejection control for virtual synchronous generator," *Int. J. Electr. Power Energy Syst.*, vol. 123, Dec. 2020, Art. no. 106144.
[22] Z. Li, Q. R. Hao, S. Y. Wang, and M. Y. Guan, "Research on nonlinear decoupling control of MMC based on state feedback exact linearization," *Chin. J. Elect. Eng.*, vol. 39, no. 12, pp. 3646–3659, 2019.
[23] Y. G. Guo, "A sliding mode control strategy for photovoltaic inverters based on state feedback precise linearization decoupling," *Automat. Instrum.*, vol. 36, no. 4, pp. 30–34 and 56, 2021.
[24] Y. Liang, Y. He, and Y. Niu, "Microgrid frequency fluctuation attenuation using improved fuzzy adaptive damping-based VSG considering dynamics and allowable deviation," *Energies*, vol. 13, no. 18, p. 4885, Sep. 2020.
[25] Y. Xu, H. Nian, Y. Wang, and D. Sun, "Impedance modeling and stability analysis of VSG controlled grid-connected converters with cascaded inner control loop," *Energies*, vol. 13, no. 19, p. 5114, Oct. 2020.
[26] B. Duan, C. Zhang, M. Guo, and G. Zhang, "A new digital control system based on the double closed-loop for the full-bridge inverter," *Int. J. Adv. Manuf. Technol.*, vol. 77, nos. 1–4, pp. 241–248, Mar. 2015.
[27] Z. Zeng, R. X. Zhao, and H. Yang, "Modeling and control of grid-connected inverters," in *Control Techniques for Flexible Grid-Connect Inverter*. Beijing, China: Science Press, 2020, pp. 55–65.
[28] C. Kalavalli, P. Meenalochini, P. Selvaprasanth, and S. S. A. Haq, "Dual loop control for single phase PWM inverter for distributed generation," *Mater. Today*, vol. 45, pp. 2216–2219, Jan. 2021, doi: 10.1016/j.matpr.2020.10.116.
[29] Y. Ma, L. Yang, X. Zhou, and X. Yang, "New double closed loop linear active disturbance rejection control of energy storage grid-connected inverter based on lead-lag correction link," *IEEE Access*, vol. 8, pp. 105411–105425, 2020, doi: 10.1109/access.2020.3000309.
[30] S. Bouri, T. Boudaoud, and T. Boudjelal, "PI controller for controlling a three-phase inverter of a PV system connected to the electrical network," *Acta Electrotechnica et Inf.*, vol. 21, no. 3, pp. 11–18, Dec. 2021, doi: 10.15546/AEEI-2021-0014.

[31] S. Sathish Kumar, R. Ramkumar, S. Sivarajeswari, D. Ramya, T. Subburaj, and M. Sankoh, "Performance enhancement of a three phase boost-cascaded fifteen level inverter using the PI controller," *Math. Problems Eng.*, vol. 2022, pp. 1–17, May 2022, doi: 10.1155/2022/3888571.

[32] S. Huang, X. Guo, R. Wang, and Y. Mei, "A SVPWM algorithm based on four-switch three-phase inverter for PMSM under the imbalance of bus capacitor voltage," *J. Power Electron.*, vol. 21, no. 12, pp. 1812–1822, Dec. 2021, doi: 10.1007/S43236-021-00324-7.

[33] J. Pígl and R. Cipín, "Dynamic model of medium voltage vacuum circuit breaker and induction motor for switching transients simulation using Clark transformation," *Energies*, vol. 16, no. 3, p. 1020, Jan. 2023, doi: 10.3390/EN16031020.

[34] N. K. Sakthivel and S. Sutha, "A novel algorithm of MGWO-based PI controller for a single-stage grid-connected flyback inverter with ZVS," *Automatika*, vol. 63, no. 1, pp. 64–77, Jan. 2022, doi: 10.1080/00051144.2021.2005288.

FANNIE KONG was born in Guangxi, China, in September 1973. He received the Ph.D. degree in power system and automation from Guangxi University, in September 2013. He is currently a Professor with the School of Electrical Engineering, Guangxi University. His main research interests include turbine control, joint optimal operation of cascade hydropower stations, intelligent power generation, and power system stability and control.

HAOCHEN ZHANG was born in Jiyuan, China, in March 1998. He is currently a Graduate Student. His main research interest includes VSG modeling and control.

WU ZHUOLIN was born in Guangxi, China, in July1998. He is currently a Graduate Student. His main research interest includes hydro-turbine modeling and control.

GUO ZHUANGZHI received the Ph.D. degree. He is currently a Professor. His main research interests include power system analysis and control, and distribution network automation.